Electrifying Thermal Loads vs. Installing Batteries: A Case Study on Fast Frequency Resource Potentials of the Victorian Power System

Johanna Vorwerk*, Isam Saedi‡, Pierluigi Mancarella ‡,and Gabriela Hug*
* Power Systems Laboratory, ETH Zürich, Zürich, Switzerland
‡Department of Electrical and Electronic Engineering, The University of Melbourne, Melbourne, Australia
vorwerkj@ethz.ch

Abstract—**Literature suggests different technologies and control algorithms to counteract the decrease in system damping and inertia caused by the increasing penetration of inverter-interfaced resources in renewable power systems. Published studies generally focus on comparing different control mechanisms for a single technology and examine a limited number of operating conditions. Technology comparisons are typically limited to small test cases, base on assumptions that no longer hold in renewable-rich systems or are solely based on literature reviews. This work thoroughly compares fast-frequency reserve provision from inverter-based active thermal loads (ATLs) against battery storage. As such, we employ a large-scale multi-level test case representing the future Victorian power system and link steady-state and dynamic analysis. We examine the frequency and voltage performance following distinct disturbances for five days with hourly resolutions. The results suggest that the potential for electrifying residential heating demand in Victoria is enormous and can significantly enhance frequency metrics. Generally, the improvements achieved with the aggregation of ATLs are similar or even higher than employing a large battery.**

Index Terms—**Fast-frequency reserve, inverter-based heat pumps, battery energy storage, renewable power systems**

I. INTRODUCTION

Several solutions, such as grid-forming and grid-following control of Voltage Source Converters (VSCs) or fast demand response strategies, have been suggested in the literature to cope with the decline in system inertia and damping caused by the increasing penetration of Inverter-Based Resources (IBRs) [1]. While batteries and thermal loads have been proposed in numerous publications to provide Fast-Frequency Reserve (FFR), the literature is generally limited to comparing the regulatory landscape or different control modes for the same technology. For example, [2,3] review global grid standards for FFR provision, list implemented battery projects, and pinpoint technical issues associated with FFR provision in IBR-rich power systems. Similarly, [4] provides an overview of grid-forming battery storage projects. The work in [5] reviews technological solutions for frequency regulation in IBR-rich systems and provides a deep-level comparison of battery models for frequency reserve studies.

Comparisons of different resource technologies are typically limited to small test cases or are subject to assumptions that no longer hold in renewable-rich power systems [5]. In addition, most control concepts are only tested for a limited number of operating conditions, model the load-side contributions as large aggregations or are restricted to the Transmission Network (TN) level. However, some resource types, e.g., distributed batteries and demand response, are located in subordinated Distribution Networks (DNs). While [6,7] suggest control algorithms to ensure reliable DN-operation with device aggregations, the considered time scales are not suitable for FFR. Consequently, the effect of supplying an FFR-service at TN level through DN resources is not assessed [8].

Steady-state analysis of renewable power systems shows that operating conditions are subject to high variability throughout the day, even more so with the integration of additional demand from electrified heating. For example, [9] examines how the electrification of heating via heat pumps in Victoria alters the steady-state operation. Similarly, [10] assesses the electrification of heating demand for the Italian power system and depicts variable daily patterns. With these changing operating conditions, inertia levels and system strength change accordingly. While some works, e.g. [11,12], acknowledge the impact of time-varying penetrations of Inverter-Based Generation (IBG) on system strength and stability, studies that link steady-state and dynamic analyses are missing.

This paper addresses the abovementioned shortcomings and presents a large-scale multi-level case study on the power system of Victoria (VIC). The conducted study extends the recent steady-state analysis in [9,13], where the impact of electrifying formerly gas-based thermal loads on the steady state of the VIC power system is examined. Here, we aim to assess the contribution of the electrified thermal load to frequency dynamics if these are implemented in a grid-supporting fashion, called Active Thermal Loads (ATLs) in the remainder of this paper. Furthermore, their performance is compared to that of grid-scale batteries. As such, the contributions of the presented work are as follows:

- We employ a straightforward method to link steady-state and dynamic studies. The method consists of three distinct steps and uses an Optimal Power Flow (OPF) solution as input for the dynamic simulation.
- We use a large-scale test case with multiple DN and TN layers to run extensive dynamic studies on a representation of the VIC power system. We simulate three different electrification levels of residential thermal loads and two battery scenarios for five exemplary days with hourly resolution.
- Finally, the performance of all scenarios is assessed with respect to steady-state and dynamic performance metrics. The results highlight how a system's steady-state and dynamic

performance are linked while providing detailed insights into the reserve provision with batteries and ATLs.

In short, the key aim of the presented work is to answer the following two research questions: (1) How much can the replacement of residential gas-based heating with inverter-interfaced heat pumps that employ FFR help frequency response in VIC? (2) Is electrification of thermal loads equally efficient to improve frequency dynamics as deploying battery storage?

The remainder of this paper is structured as follows: The scenarios for the case studies are detailed in Section II, while Section III describes the applied method. Section IV provides insights into the test case and the ATL model. Then, steady-state and dynamic results are presented in Section V. Finally, Section VI concludes the work.

II. SCENARIOS

This work analyzes dynamic simulations based on realistic scenarios of the future VIC power system, which is a part of the interconnected eastern Australian power system. For this purpose, carefully selected scenarios that assess the impact of electrifying residential heating demand in VIC are examined. All scenarios were selected to represent the projected future situation of the VIC power system. This section details the setup and layout of the studied scenario tree. Since the presented study continues the work presented in [9,13], the chosen scenarios are similar. Fig. 1 provides an overview of the scenario tree detailed in the remainder of this section.

A. AEMO's 2020 Integrated System Plan

Our case studies comply with the 2020 Integrated System Plan (ISP) provided by Australian Energy Market Operator (AEMO) in [14]. In its reports, AEMO assesses five scenarios to trace
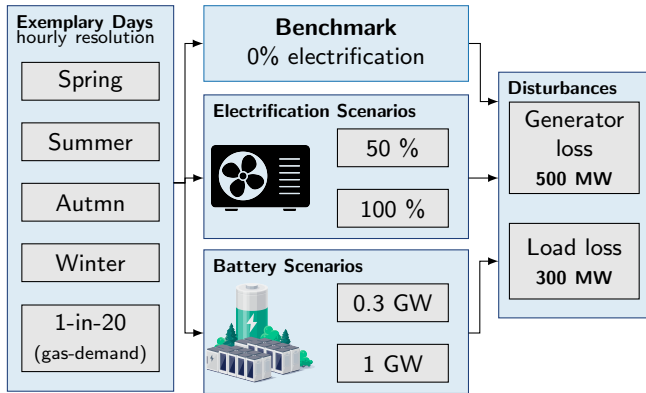

Fig. 1. Overview of the scenario tree: Each exemplary day is considered with hourly resolution, i.e. 24 operating points.
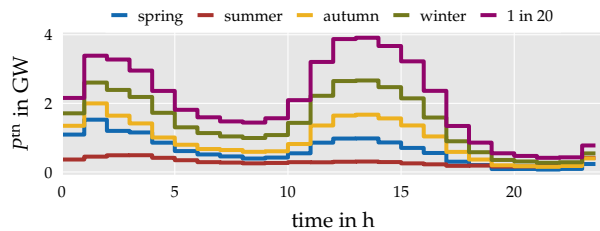

Fig. 2. Electrified load P^{th} per representative day for the 100% electrification scenario. The depicted values halve for the 50% case.

different speeds of the energy transition. Our work builds on the AEMO Step Change scenario that is the most aggressive transition. It exhibits high uptakes in distributed energy resources, demand, and variable Renewable Energy Sources (RES). As such, it incorporates a 50% renewable energy target in VIC by 2030. Furthermore, it exhibits the highest net market benefits. All assumptions, inputs, and outcomes are available in [14, 15].

This work assesses the potential of electrifying residential heating demand for five representative days under the Step Change scenario for the projected generation mix of 2025. Electricity demand and RES output forecasts for the representative days and months are obtained from the 2020 ISP in [15]. The electric system model provided in [16] is adjusted to account for the 2025 generation mix, the augmentation of interconnectors, and internal network extensions.

B. Electrification Scenarios

The studies are conducted for five different *gas* demand days, which are obtained from actual historical data provided in a temporal resolution of 1 hour. Generally, the average daily gas demand in VIC varies from $280\,\mathrm{TJ/day}$ in summer to $900\,\mathrm{TJ/day}$ in winter. The peak gas demand is around $1200\,\mathrm{TJ/day}$. Within each day, the gas demand for space heating may vary significantly. Such intra-day variations are predominantly affected by outdoor temperatures and time of day [9,13]. The following representative days have been selected to depict most of these variations:

- Average *spring* demand on Oct, 21th 2019
- Average *summer* demand on Dec, 22nd 2019
- Average *autumn* demand on May, 15th 2019
- Average *winter* demand on July, 17th 2019
- *1-in-20* peak gas demand on August, 9th 2019

where the cursive parts denote the scenarios for the remainder of the paper. Each representative day is projected to 2025 under the AEMO 2020 ISP Step Change scenario. Different electrification levels of gas-based residential space heating and domestic hot water supply are considered. These include a base case scenario with no electrification, referred to as 0% or benchmark, medium electrification at 50%, and high electrification at 100%. Details on the gas demand breakdown into different sectors and the procedure for electrification of the thermal demand are provided in [9,13].

An overview of the resulting electrified thermal demand, i.e. the additional active power demand stemming from the electrification, is depicted in Fig. 2 for the 100% scenario. As expected, the electrified thermal load P^{th} is lowest during summer and highest in the colder months, peaking around $4\,\mathrm{GW}$ active power demand for the 1-in-20 demand scenario. Considering the five representative days with hourly resolution and three electrification scenarios, 360 operating points for the VIC power system are obtained.

C. Battery Scenarios

Like the electrification scenarios, the battery sizing reflects the actual situation in the VIC power system. Currently, several large projects are online or planned. For example, the VIC big battery project installs a $300\,\mathrm{MW}$ battery in the Moorabool power station [17]. Other battery projects close to VIC are located in South Australia $(100\,\mathrm{MW})$ [18] and planned in New South Wales $(700\,\mathrm{MW})$ [19]. But, the storage capacity is not only employed for FFR. Indeed, the ISP 2022, provided in [20], projects storage

capacities for specific grid services. The plan differentiates shallow storage required for short-term control from longer-term service provisions required to balance intra- or even inter-daily load variations. It projects $1\,\mathrm{GW}$ of storage for short-term services in the entire National Electricity Market (NEM).

Considering these projections, the studies are conducted for two battery sizes: a battery with (1) $300\,\mathrm{MW}$ capacity to reflect the current grid-scale storage availability within VIC, and (2) $1\,\mathrm{GW}$ capacity to reflect the planned FFR storage capability of the NEM. The batteries idle in the pre-fault state, hence do not alter the pre-fault system operating conditions.

D. Selected Disturbances

Since the presented case study focuses on frequency dynamics, trigger disturbances are to be selected. Typically, the worst case for frequency stability is the loss of the largest generator in the system. Thus, the first considered disturbance is the loss of a $500\,\mathrm{MW}$ coal-fired generator. In addition, a load drop of $300\,\mathrm{MW}$ is studied. This magnitude corresponds to the spinning reserve required in VIC and is selected such that for the base case, all spinning reserve needs to be activated. With these two disturbances, a total of 720 dynamic simulations are conducted.

III. Algorithmic Methodology

The flow chart in Fig. 3 details the applied method advanced from the approach in [9]. The first stage obtains an optimal electricity dispatch per scenario: per electrification per hour of each day. It is based on inputs such as TN and gas network infrastructures, electricity and gas demand profiles, renewable forecasts, and generation information. A unit commitment with a strengthened DC-OPF model provides all generators with optimal active power setpoints. These are used in the second stage to prepare the power system dynamic studies. As such, the 2nd stage disaggregates the TN nodal demand to subordinated DNs that are only considered in the last two stages. A complete Newton-Raphson method provides a full power flow solution, including reactive power setpoints of all generators, additional voltage regulators, and nodal voltage magnitudes and angles. Stage 3 uses the obtained solution and runs dynamic simulations for the two selected contingencies. Dynamic models and their parameters for all system components, such as generators, exciters, turbines, governors, loads, wind turbines, and PV systems, are employed for this last step. Finally, stability indicators are evaluated to compare the performance of different scenarios. The remainder of this section describes each stage of the method and its implementation in more detail.

A. Stage 1: Optimal Energy Dispatch per Scenario

The first stage provides the optimal energy dispatch of the generation mix and the curtailment of RES for each scenario at the TN level. It implements a Unit Commitment (UC) with a strengthened DC-OPF model that estimates system losses, considers spinning reserve, and is solved over a 24-hour scheduling horizon with an hourly resolution for each representative day, as developed and executed in [9,13,21]. The reader is referred to [21] for a detailed formulation of the optimization algorithm.
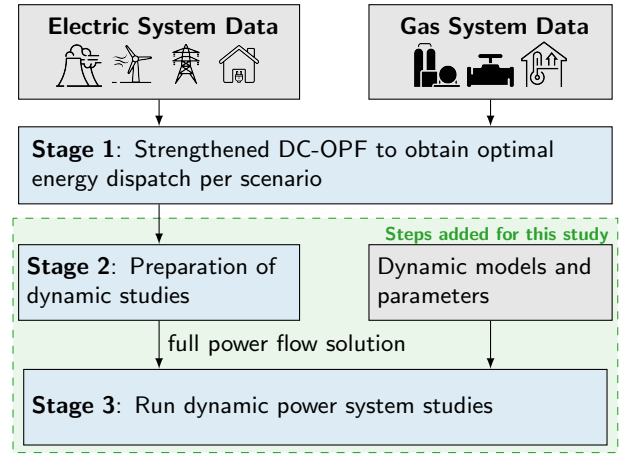

Fig. 3. Overview of the algorithmic process (The chart was expanded and adapted from [9]).

B. Stage 2: Preparation of Dynamic Power System Studies

A complete power flow solution, including all grid levels, is required to initialize the dynamic studies. Stage 2 obtains such a solution. However, the Newton-Raphson algorithm requires further inputs. Since Stage 1 only uses the net active load per TN node, further disaggregation to the DN buses is essential. Also, reactive power is not considered in the DC-OPF formulation. Hence, assumptions are required to determine reactive power demand.

1) Disaggregation of Load: From the inputs to the first stage, the nodal thermal active power demand $P_{i,s}^{\mathrm{th}}$ and the remaining electric power consumption, referred to as background load, P_s^l are known per scenario s. Hence, the total nodal load at the i-th TN bus for the s-th scenario $P_{i,s}$ is

$$P_{i,s} = \kappa_i P_s^l + P_{i,s}^{\mathrm{th}} = P_{i,s}^l + P_{i,s}^{\mathrm{th}}, \tag{1}$$

where κ_i is the fixed background load share of the i-th TN node. These fixed load shares are provided in [16].

The TN nodal background and thermal load are further disaggregated for the dynamic studies. The entire thermal load is consumed in subordinated DNs because the electrified heating scenarios only integrate residential demand. On the contrary, shunts connected to the TN buses partially consume the background load to account for industrial and other large consumers. Thus, the shunt active $P_{i,s}^{\mathrm{sh}}$ and the DN nodal active power consumption $P_{ij,s}$ are

$$P_{i,s}^{\mathrm{sh}} = \kappa_i^{\mathrm{sh}} P_{i,s}^l = \kappa_i^{\mathrm{sh}} \kappa_i P_s^l, \tag{2}$$

$$P_{ij,s} = \kappa_{ij} P_{i,s}^l + \kappa_{ij} P_{i,s}^{\mathrm{th}} = \kappa_{ij} \kappa_i P_s^l + \kappa_{ij} P_{i,s}^{\mathrm{th}}, \tag{3}$$

where κ_i^{sh} is the constant power share of the shunt and κ_{ij} denotes the constant share of power consumed by the j-th DN node subordinated to the i-th TN bus, respectively. The same active power distribution is used for background load and thermal load. Note that the sum of load shares at one TN bus must be unity, i.e. $\kappa_i^{\mathrm{sh}} + \sum_{j \in \mathrm{DN}_i} \kappa_{ij} = 1$, where DN_i includes all DN buses subordinate to the i-th TN node. A system-wide constant power factor is assumed because no information on reactive power is provided from Stage 1 or the input data. Since the added ATLs are interfaced with inverters and operate at unity power factor, the reactive power is computed using the background active power demand.
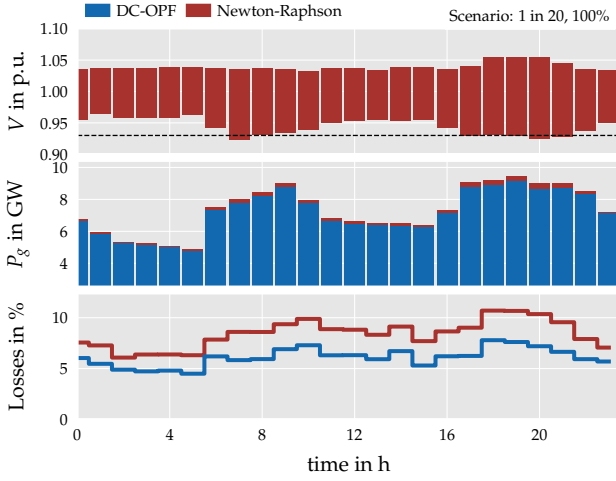
Fig. 4. Comparison of the DC-OPF solution to the full Newton-Raphson for the 1-in-20 electrified demand day with 100% electrification. The dotted line in the voltage magnitude plot corresponds to $\underline{v} = 0.93$ p.u.

Fig. 5. Graphic interpretation of the Undervoltage Score (UVS) for a single bus with $\underline{v} = 0.93$ p.u.

2) Full Power Flow Solution: The results from the disaggregation algorithm and Stage 1 are combined to obtain a complete power flow solution and used to initialize the dynamic studies. The power flow computation software Artere [22] is used. All generator buses, including those connecting IBG and excluding the slack bus and nodes connecting Static VAR Compensators (SVCs), are treated as PV buses that actively participate in voltage control. All other buses are of PQ type. With Artere, all outputs for the next stage are obtained, namely, active and reactive power setpoints for all generators and voltage magnitudes and angles of all buses.

The DC-OPF and the Newton-Raphson solution do not perfectly match despite including system losses in the DC-OPF. The overall system losses increase by up to 2% of the total load for the Newton-Raphson algorithm. The generator at the slack bus can cover these additional losses in all cases. Fig. 4 showcases the comparison for one exemplary day and electrification scenario. This day exhibits the highest overall electric load.

In addition, Fig. 4 depicts the voltage ranges throughout all grid layers. The voltages of all nodes are within the shaded region. The voltage is less than 0.93 p.u. only for a few cases and remains within the limits of 0.9 p.u. to 1.1 p.u. at all times.

C. Stage 3: Dynamic Power System Studies

Dynamic studies for the two selected TN faults employing the previously obtained complete power flow solution and additional dynamic models and their parameters are performed. The dynamic system is implemented in Ramses [23] and executed on a server using parallelization to reduce computation times. For the quantitative assessment of the dynamic simulations, frequency and voltage stability indicators are introduced to evaluate each scenario.

1) Frequency Indicators: The selected frequency stability indicators indicate how well the system responds to the given disturbance but cannot determine whether the system is stable. They are rather a comparative measure to assess the different operating conditions. The selected frequency indicators include (1) the maximum Center-of-Inertia (COI) frequency deviation $\Delta f_{\text{coi}}^{\text{max}}$, and (2) and the steady-state COI frequency deviation $\Delta f_{\text{coi}}^{\text{ss}}$. Since the dynamic simulations are performed for a fixed simulation time to
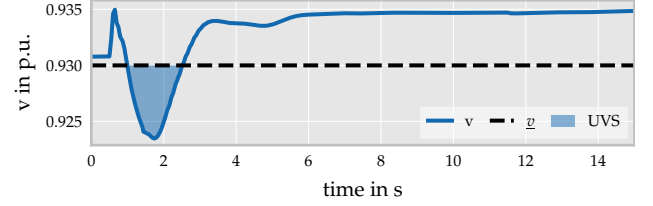
keep the computational effort within bounds, a pragmatic approach to quantify the steady-state frequency deviation is selected. The simulations are conducted for $20\,\text{s}$, while the contingency occurs at $t = 1\,\text{s}$. Since only the primary frequency response is reacting, and no integrative control is active, the frequency typically has settled at this point. Thus, the COI steady-state frequency deviation is evaluated at $t = 20\,\text{s}$, that is, $19\,\text{s}$ after the contingency occurred. Preliminary studies assessed the Rate-of-Change-of-Frequency (ROCOF) as an additional indicator. However, neither batteries nor heat pumps significantly affected the ROCOF-levels, which is to be expected. While both control strategies are capable of supplying a fast response, the implemented ROCOF estimation technique is still too slow for effective ROCOF reduction and hence mirrors the problem of supplying virtual inertia through measurement-based ROCOF-proportional control.

2) Voltage Indicators: In addition to the frequency metrics, voltage indicators are evaluated. Like the frequency indicators, these do not assess stability but serve as a comparative metric. The selected indicators include (1) the maximum (v^{max}) and minimum (v^{min}) voltage magnitudes in p.u., and (2) the undervoltage and the overvoltage score. The latter scores account for the severity of a voltage violation across the entire system. Fig. 5 graphically defines the Undervoltage Score (UVS) for a single bus. It equals the area, or integral, where the voltage magnitude is lower than the voltage magnitude bound $\underline{v}$. The UVS of the entire system is the sum of all these areas, i.e.

$$\text{UVS} = \sum_{i \in \mathcal{B}} \int_{t_{v_i \leq \underline{v}}}^{t_{v_i \geq \underline{v}}} (\underline{v} - v_i(t))\, dt, \quad (4)$$

where $\mathcal{B}$ is the set of all buses. Similarly, the Overvoltage Score (OVS) is defined as

$$\text{OVS} = \sum_{i \in \mathcal{B}} \int_{t_{v_i \geq \overline{v}}}^{t_{v_i(t) \leq \overline{v}}} (v_i(t) - \overline{v})\, dt. \quad (5)$$

Both scores equal 0 when no bus exceeds the voltage limits $(\underline{v}, \overline{v})$ at any time. The selected voltage magnitude bounds are $\underline{v} = 0.93$ p.u. and $\overline{v} = 1.07$ p.u., and correspond to the limits selected during the diversification procedure of the large test case. A trapezoidal rule computes the integral because the obtained time-domain responses are discrete signals.

IV. TEST CASE & DYNAMIC MODEL

This section provides insights into the dynamic modeling of the test case that includes the $22\,\text{kV}$ to $500\,\text{kV}$ TN and DN layers. It further details the ATL and battery model.

A. Test Case

The test case is a combination of the TN-layer employed in Stage 1 and the Australian sample DN system published in [24]. A full description of the test system is available in [25].

The VIC TN layer comprises 125 buses, 139 transmission lines, five interconnections to neighboring states, and 51 transformers. The generation mix comprises six hydropower plants, six large-scale PV power plants, 17 wind farms, and 11 coal- and gas-fired power plants, totaling 40 generators. The installed generation capacity is $15.2\,\text{GVA}$. Since no information on voltage control is publicly available, all voltage-controllable devices control their terminal voltage to $1\,\text{p.u.}$ Conventional generators are modeled by standard 5th and 6th order Synchronous Machine (SM) and are equipped with governors, exciters, and Automatic Voltage Regulators (AVRs). In contrast, IBGs are modeled with the WECC models from [26] and control their reactive power setpoint through a voltage-reactive power droop. They do not provide frequency reserve. Several SVCs are included in the system. While their impedance is adjusted during the full Newton-Raphson, it is constant for the dynamic simulation. The same assumption holds for all tap changers. All machinery is considered with standard dynamic models as outlined and parameterized in [25].

One or multiple DN feeders with 93 nodes each are connected to each TN node. While the electrified thermal load is distributed with the constant load shares defined in Section III-B1, some background load is consumed by TN shunts. The DN layer consists of 203 independent feeders and 18880 buses. In other words, the test case includes 18880 individual ATLs and 18880 background loads. Each background load is modeled as an induction machine and an exponential load model as described in [25]. Note that the background load consumption of the DN layer corresponds to the net load. Distributed generation, like residential PV, is not considered separately because no data was available.

B. ATL Model

The heat pumps are modeled by a universal ATL model. Fig. 6 provides an overview of the outermost control layer, where the blue block represents an even more detailed Differential-Algebraic Equation (DAE) model including inverter control dynamics of the ATL. The model was derived in [27], extended in [28], and is detailed in [25]. We refer the reader to the mentioned publication for a definition of all variables. The following adaptions apply: In [28], the ATLs provided solely a frequency-proportional droop with a constant gain. In this work, the frequency support block is replaced with the version in Fig. 7. Besides the frequency-proportional reaction, a ROCOF-proportional droop is added to achieve a faster response immediately after the fault occurs. In addition, the droop gains are no longer constant but depend on the pre-fault operation. The piecewise-linear droop gain d_f is computed depending on the individual unit's pre-fault operating point p_0 and available reserve ($p_{\min}, p_{\max}$) with:

$$d_f^{up} = \frac{p_{\max} - p_0}{f_{\max} - f_n} f_n, \qquad d_f^{dn} = \frac{p_0 - p_{\min}}{f_n - f_{\min}} f_n, \qquad (6)$$

where $f_{\min}$ and $f_{\max}$ denote the frequency values at which the maximum reaction should occur. When the pre-fault consumption is high, the gain to increase the load further d_f^{up} is small, while the gain to drop load d_f^{dn} is large. Furthermore, the ATLs have a
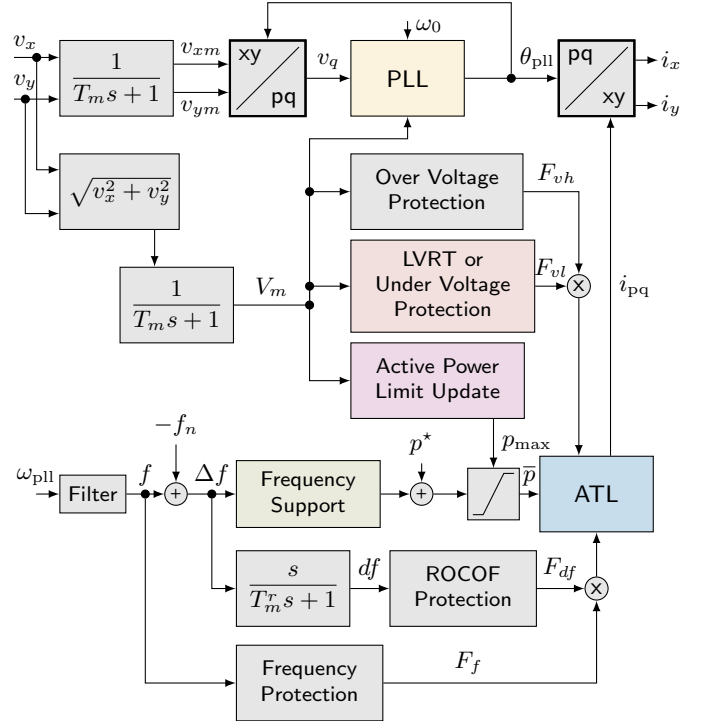
Fig. 6. Grid-level control layer of one ATL unit. The blue block represents the universal model formulated in [27].
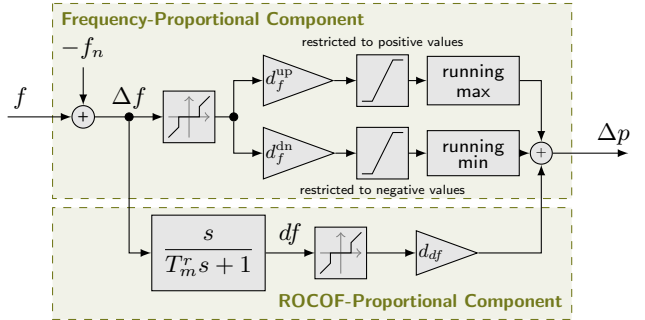
Fig. 7. Block diagram of the ATL frequency support. The droop gains depend on the initial operating conditions.

sustained droop, as indicated by the running min and max blocks in Fig. 6. Once the maximum post-fault reaction is reached, the unit continues to provide that amount until the fault is cleared. With this control configuration, the support from the DN layer is maximized while being more grid-friendly than constant droop gains. For a comparison of different control modes and further details regarding the control formulation and parameterization of all units, the reader is referred to [25].

C. Battery Model

For both battery scenarios, the battery does not charge or discharge in the pre-fault steady-state and is initialized at 50 % State of Charge (SOC) to ensure no limits are reached. Hence, adding the battery does not alter the pre-fault system's operating point. The battery is modeled as a single unit in both cases and connects to a TN bus in VIC. The WECC battery model from [29] applies. The battery is added to the reference system, i.e. the 0 % electrification scenario. It provides frequency-proportional droop
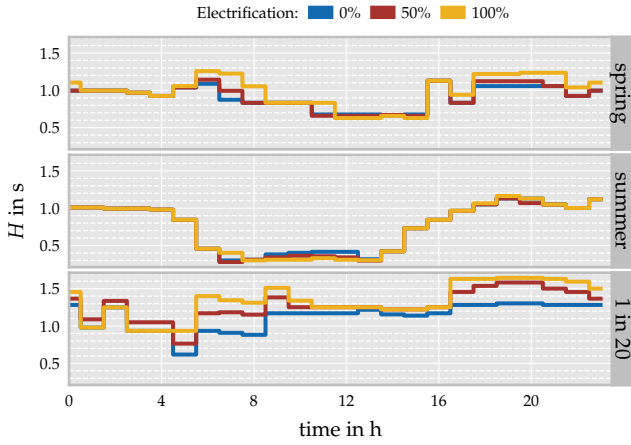
Fig. 8. Overall system inertia constant H scenario for selected representative days.
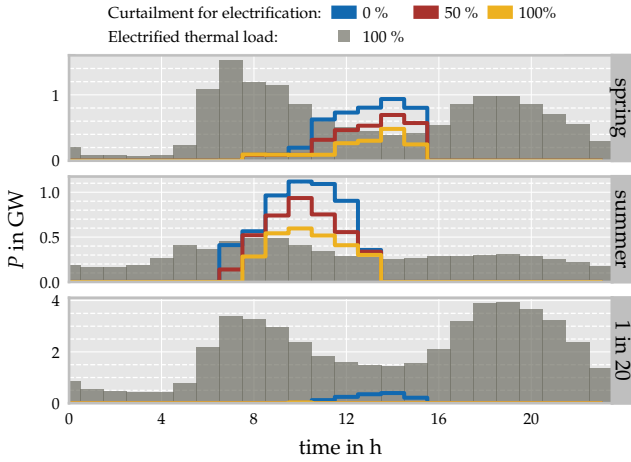

Fig. 9. Overall curtailment of RES (PV and Wind power) and electrified thermal load for selected exemplary days. Note the different scaling of the ordinate for the different days.

with a constant gain and does not support voltage to limit its effect on frequency performance.

V. Case Study Results

Before illustrating and analyzing the dynamic performance, this section clarifies some steady-state phenomena relevant to the dynamic studies.

A. Steady-State Analysis

The added heat pumps change the steady state of the power system. While a thorough analysis of steady-state metrics for some of the exemplary days is already provided in [9, 13], here we evaluate metrics that are relevant to the dynamic studies, such as the system inertia and RES curtailment. Note that no voltage violations were observed in the steady state.

For this assessment, the rotational inertia constant H of the system is evaluated with

$$H = \Sigma_{g \in \mathcal{G}_s} H_g S_{g,n} \left(\Sigma_{g \in \{\mathcal{G}_s, \mathcal{R}\mathcal{G}_s\}} S_{g,n} \right)^{-1}, \quad (7)$$

where $\mathcal{G}_s$ is the set of online synchronous machines, and the $\mathcal{R}\mathcal{G}_s$ includes all online renewable generators for scenario s. The

individual generator inertia constants and nominal powers are denoted by H_g and $S_{n,g}$ respectively.

Fig. 8 indicates significant variation in system inertia throughout the exemplary days but also reveals seasonal and electrification-level-dependent trends. Daily variations are pronounced during summer, when RES generation is highest. Then, the inertia constant varies within $0.3\,\mathrm{s}$ to $1.7\,\mathrm{s}$. Daily variations are similar when the load is high, e.g., during the cold months, but the inertia levels increase compared to summer. Also, inertia levels, in general, rise for increased electrification of thermal load since the additional load is covered by conventional generation. However, inertia reduces with high electrification during the midday of spring and summer. Considering the curtailment of RES, Fig. 9 provides insights into this counter-intuitive finding. Previously curtailed RES are turned on to cover the increased load. When the added load is mainly covered by IBGs, the overall system inertia reduces. Yet, the magnitude of inertia reduction is minor compared to the variations in inertia during high-demand days.

B. Dynamic Simulation Analysis

This section presents the quantitative analysis comparing the different electrification levels to the frequency reserve supplied by batteries. Simulations are performed for all scenarios summarized in Fig. 1. The 0 % electrification scenario provides the benchmark. This section first illustrates exemplary time-domain results for single units and system-level frequency and voltage, followed by an analysis of selected frequency and voltage indicators.

1) Exemplary Time-Domain Performance: The sum of the individual responses impacts the frequency and voltage at the system level, as exemplarily depicted for the generator loss for one specific day and time in Fig. 10. The sum of all reserve contributions from ATLs or the batteries, referred to as ΔP_x, and the COI frequency deviation are presented. The maximum and
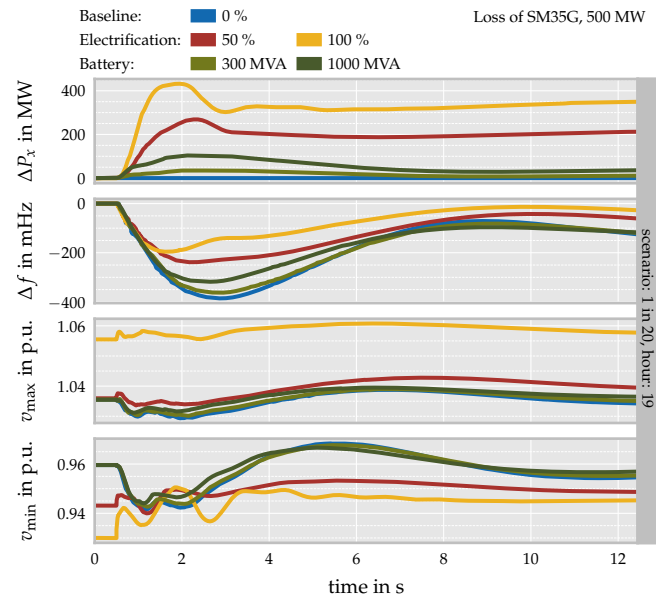

Fig. 10. System-level exemplary time-domain response for the different reserve scenarios in case of a loss of generation: Overall control reserve activation per technology ΔP_x, frequency deviation Δf and maximum and minimum voltages v_{max} and v_{min}.

minimum voltage magnitudes are acquired per time step rather than displaying the magnitude at specific buses.

Fig. 10 suggests that any added reserves improve the frequency, whereas electrification performs best. While the small battery only advances the frequency nadir by $23\,\mathrm{mHz}$, the large battery results in a maximum deviation around $300\,\mathrm{mHz}$. In contrast, electrification reduces the frequency nadir by $147\,\mathrm{mHz}$ and $190\,\mathrm{mHz}$. In the latter case, with $100\,\%$ electrification, almost the entire generator loss is covered by responding ATLs.

Furthermore, Fig. 10 highlights the different control settings. The ATL response is faster than the batteries due to the ROCOF-proportional component. In addition, the sustained droop ensures a high post-fault steady-state reserve contribution.

While the battery does not impact the voltage magnitudes significantly, the electrification scenarios invert the initial response. Instead of decreasing, the minimum voltages rise right after the disturbance due to the fast reduction of ATL demand in the transient phase. The maximum voltage magnitudes are relatively similar except for $100\,\%$ electrification. Here, imports are required, and further investigation of the steady state indicates that imports across the interconnectors correlate with high voltages. Note that additional generators are switched on for the electrification cases that change the voltage profile across the system.

2) Frequency Metrics: This section provides a quantitative analysis of the frequency metrics. It further highlights the correlation of the frequency metrics and ATL pre-fault loading.

Fig. 11 displays the expected maximum and steady-state frequency deviation for a generation loss in all scenarios. The bars reflect the variance occurring within each exemplary day. The mean and variability of the frequency undershoot vary significantly for the benchmark scenario across the different exemplary days, highlighting the need to consider different operating conditions during frequency stability studies. The mean deviation consistently exceeds $400\,\mathrm{mHz}$ in the base case. The lowest mean in maximum frequency deviations is below $300\,\mathrm{mHz}$ and is achieved by the high electrification scenario when the initial load is high, i.e. for autumn, winter, and the 1-in-20 days. In summer, the ATLs are less effective and only reduce the mean to $370\,\mathrm{mHz}$. Still, the $50\,\%$ electrification and large battery exhibit similar performance. In contrast, the batteries' improvement is more predictable and steady, and the mean of the maximum deviation stays in the same range. Fig. 11 further suggests that the variability is affected by electrification. While high electrification increases the variation in maximum frequency deviation compared to the benchmark for some days, the opposite holds during summer. Generally, the summer day exhibits the highest variation in all cases, which is due to the load and generation profile. As the previous steady-state analysis suggested, the system is weakest during midday in summer but still has larger inertia at night.

Fig. 11 permits similar conclusions for the steady-state frequency deviation, although the differences in the mean are more minor, as indicated by the smaller spread. Any reserve improves the performance, and major improvements occur for high-loading conditions. The advancement by batteries is more consistent throughout the exemplary days. However, the scenarios with little ATL demand (summer and spring) still achieve a response similar to that of the large battery.
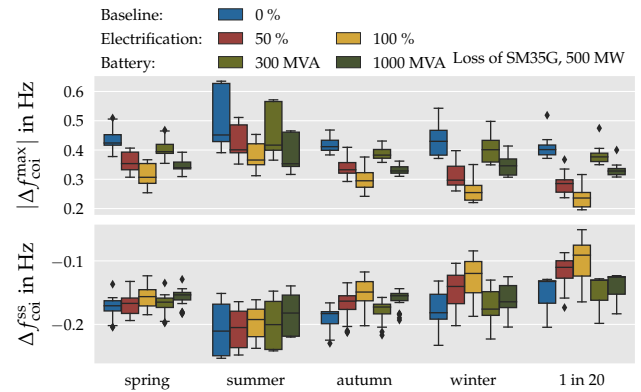

Fig. 11. Boxplot of the frequency indicators for all exemplary days in the case of a generator loss.
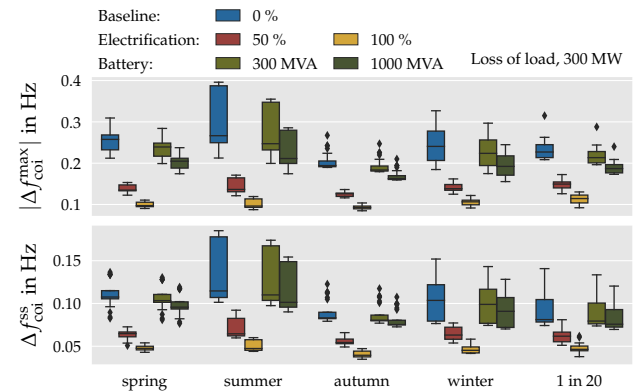

Fig. 12. Boxplot of the frequency indicators for all exemplary days in the case of a load loss.

The most important finding here is that ATLs perform as well as the large battery in summer, when the potential offered by ATL is low. During these times, little heating is required, so the potential in terms of droop gain to reduce the load further in response to a generator outage is small. Yet, it is still sufficient to stabilize the simulated generator outage and perform as well as the batteries.

Fig. 12 shows the values for frequency metrics obtained during load loss. Again, variations are dependent on the specific exemplary day but are generally of a smaller magnitude than for the generator outage. The improvements achieved by electrification outperform the batteries on any day. This holds for both the maximum and steady-state frequency deviations. In addition, the variance is reduced for the electrification scenarios for all exemplary days compared to the benchmark, reducing uncertainty in maximum and steady-state frequency deviations. In contrast, the batteries are subject to similar uncertainty levels as the benchmark.

The conclusions drawn from Fig. 12 must be considered cautiously. The modeling in this case study does not consider that ATL units might disconnect during warmer months and not be available for reserve. Hence, the results for warmer months are subject to change when considering this fact. However, the results for colder months are accurate since all units should be online during these periods. Note that the reserve supplied by ATLs during the cold periods (autumn, winter, and 1-in-20) is still sufficient to improve frequency metrics significantly. At these times, the droop gain to increase the load, as is required during a load loss, is small,
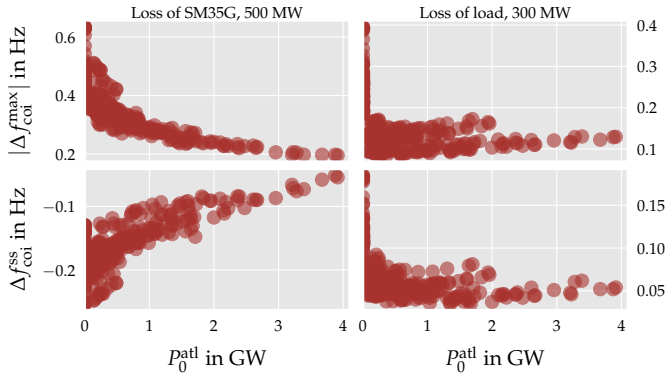
Fig. 13. Correlation of the pre-fault thermal load and the frequency indicators in the case of a generator loss on the left and load loss on the right.

potentially limiting their efficacy. Fig. 12 further suggests that the load increase provided by those ATLs is even sufficient to outperform the batteries.

The previous conclusions indicate a correlation of ATL demand and frequency metrics. Fig. 13 studies how the pre-fault ATL consumption relates to the frequency performance metrics. For the generator loss, Fig. 13 suggests an explicit dependency of pre-fault ATL consumption and frequency metrics. The dependence seems to follow an anti-proportional relation for absolute frequency deviations. In case of a load loss, some dependencies are lost and any added thermal load drastically improves the frequency metrics. Remember, this effect might be caused by overestimating reserve capabilities for a load loss in times of low ATL demand.

3) Voltage Metrics: Before analyzing the metrics, note that voltage control and the modeling of reactive power resources are potentially improper. The implemented voltage control scheme controls all voltages to $1\,\text{p.u.}$. In the actual system, voltage magnitude setpoints are different. Consequently, reactive power setpoints would adapt, and the voltage profile across the system would change. Nevertheless, we can observe some tendencies.

Fig. 14 displays the voltage magnitudes and highest UVS for all scenarios subjected to the generator outage. Voltage violations are generally undervoltages and cause the highest UVS during summer, but severe undervoltages occur during spring and winter. These undervoltages are likely caused by the adjusted generation profile. The highest RES shares occur in summer. Then, active power is transmitted over long distances from the RES locations to the load centers. The low voltages indicate that the voltage control capabilities are insufficient, and additional resources might be required.

The results indicate a strong interdependence of frequency and voltage performance since voltages are generally improved by the ATLs or a battery. An improved frequency performance leads to better voltage levels, even if the same generators are online, as is the case for the battery scenarios. The effect is dominant in a weak system, e.g. during midday in summer. This finding highlights the need to consider voltage and frequency dynamics in renewable power systems simultaneously.

For a load loss, undervoltages decline, as shown in Fig. 15. The severity of violations observed in the high electrification scenario during the winter and 1-in-20 days is significantly smaller than
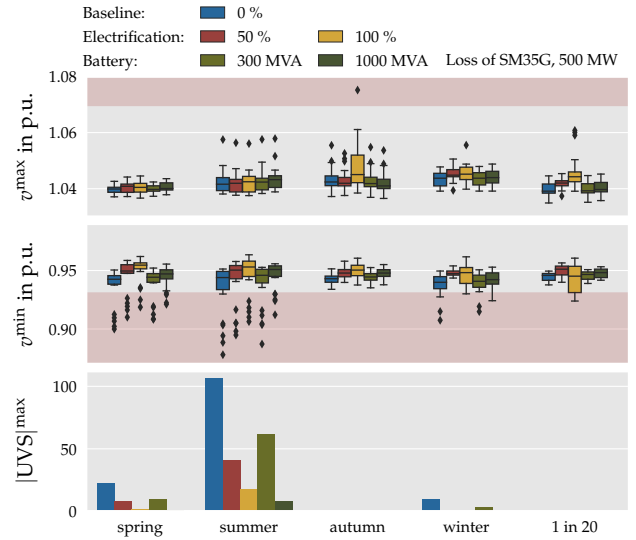

Fig. 14. Voltage indicators for all exemplary days in the case of a generator loss.
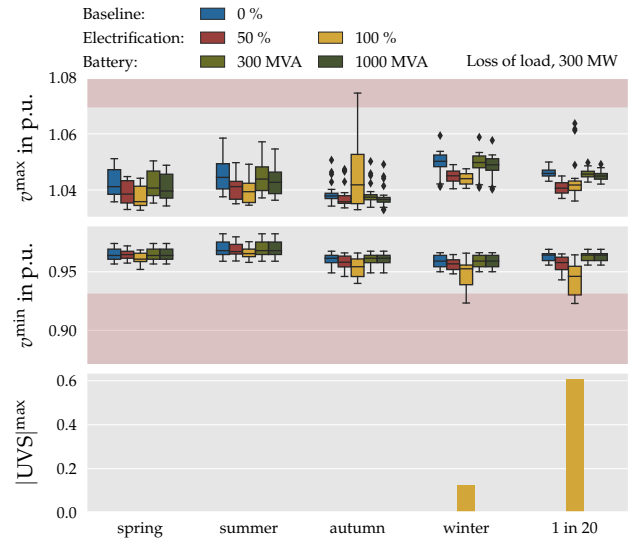

Fig. 15. Voltage indicators for all exemplary days in the case of a load loss.

for a generation loss in summer and likely caused by the high demand of the 100 % electrification case.

VI. CONCLUSIONS

The presented work compares FFR provision from ATLs against that of batteries. To this end, a large scenario-based case study is performed on an implementation of the VIC power system. The battery sizing considers actual projections by AEMO on future storage needs for short-term control services. Likewise, the added heat pumps correspond to the possible electrification amounts of residential currently gas-based hot water and space heating supply. Per design, the study links steady-state and dynamic analysis. The applied test case includes voltage levels from $22\,\text{kV}$ to $500\,\text{kV}$. Two faults, the loss of the largest generator and a load loss, are selected for the dynamic simulations. The operating points of the system correspond to five exemplary days of the VIC power system. A DC-OPF provides the optimal active power setpoints for all generators, and a full power flow establishes the initial state, including voltage magnitudes, angles, and reactive power

setpoints, for the dynamic simulation. Frequency and voltage stability indicators are evaluated for each scenario.

The case study reveals daily and seasonal patterns in the expected maximum frequency deviations. The deviations follow the level of inertia and available FFR. During summer, the frequency deviation experienced after a generator outage varies by $400\,\mathrm{mHz}$ depending on the time of day and the scenario. Correspondingly, the reserve requirements to safeguard system operation change significantly within one day. New tools are required to find and assess the weakest and most critical operating conditions.

The dynamic simulations highlight that the electrification of residential heating in VIC and its employment in FFR provision is a promising pathway to ensure stable operation in the future. Electrifying thermal loads brings several benefits while also imposing and enhancing challenges. The extensive case study suggests that the ATLs outperform the battery scenarios even when the potential FFR contribution from ATLs is small. Note that the battery does not supply a ROCOF-proportional response in the presented study, and results might change for some scenarios if they did. To this end, future work could also investigate and improve the local control mechanisms for the inverter-based thermal loads and the batteries to reach their maximum potential. Nonetheless, the results emphasize the enormous potential offered through the electrification of residential heating. The results further indicate a correlation between the pre-fault ATL demand and frequency performance. Future research should analyze how much ATL load is needed to safeguard system operation. In addition, correlation charts like the one provided could enable system operators to quickly assess the severity of a potential fault when knowing the overall load available for demand response.

The only benefit of batteries over ATLs, in terms of frequency performance in this study, is their predictability and steadiness in reserve provision. However, batteries are potentially subject to daily and seasonal patterns when required to deliver multiple services. To study such an impact, future work could expand the OPF formulation of the first stage to incorporate the multiple battery services in the optimization problem. Another interesting aspect for expanding the comparison is the inclusion of cooling and air conditioning systems, distributed batteries, and distributed PVs. These were not considered in the study since only data for residential heating was available. Additionally, future studies could enhance the voltage control scheme by gathering and considering the actual setpoints or replacing the DC-OPF formulation with an AC-OPF.

REFERENCES

[1] H. Karbouj, Z. H. Rather, D. Flynn, and H. W. Qazi, "Non-synchronous fast frequency reserves in renewable energy integrated power systems: A critical review," *Int. J. Electr. Power Energy Syst.*, vol. 106, pp. 488 – 501, 2019.

[2] L. Meng, J. Zafar, S. K. Khadem, A. Collinson, K. C. Murchie, F. Coffele, and G. M. Burt, "Fast frequency response from energy storage systems—a review of grid standards, projects and technical issues," *IEEE Trans. Smart Grid*, vol. 11, no. 2, pp. 1566–1581, 2020.

[3] D. Fernandez-Munoz, J. I. Perez-Diaz, I. Guisandez, M. Chazarra, and A. Fernandez-Espina, "Fast frequency control ancillary services: An international review," *Renewable and Sustainable Energy Reviews*, vol. 120, 2020.

[4] R. Musca, A. Vasile, and G. Zizzo, "Grid-forming converters. a critical review of pilot projects and demonstrators," *Renewable and Sustainable Energy Reviews*, vol. 165, 2022.

[5] U. Akram, M. Nadarajah, R. Shah, and F. Milano, "A review on rapid responsive energy storage technologies for frequency regulation in modern power systems," *Renewable and Sustainable Energy Reviews*, vol. 120, 2020.

[6] S. Brahma, A. Khurram, H. Ossareh, and M. Almassalkhi, "Optimal frequency regulation using packetized energy management," *IEEE Transactions on Smart Grid*, vol. 14, no. 1, pp. 341–353, 2023.

[7] S. C. Ross, G. Vuylsteke, and J. L. Mathieu, "Effects of load-based frequency regulation on distribution network operation," *IEEE Trans. Power Syst.*, vol. 34, pp. 1569–1578, 3 2019.

[8] S. Chatzivasileiadis, P. Aristidou, I. Dassios, T. Dragicevic, D. Gebbran, F. Milano, C. Rahmann, and D. Ramasubramanian, "Micro-flexibility: Challenges for power system modelling and control," in *2022 Power Systems Computation Conference (PSCC), Porto*, 2022.

[9] I. Saedi, S. Mhanna, and P. Mancarella, "Integrated electricity and gas systems modelling: Assessing the impacts of electrification of residential heating in victoria," in *2020 Australasian Universities Power Engineering Conference (AUPEC)*. IEEE, 2020.

[10] S. Bellocchi, M. Manno, M. Noussan, M. G. Prina, and M. Vellini, "Electrification of transport and residential heating sectors in support of renewable penetration: Scenarios for the italian energy system," *Energy*, vol. 196, 2020.

[11] L. Mehigan, D. Al Kez, S. Collins, A. Foley, B. Ó'Gallachóir, and P. Deane, "Renewables in the european power system and the impact on system rotational inertia," *Energy*, vol. 203, p. 117776, 2020.

[12] AEMO, "2020 System Strength and Inertia Report," 2020.

[13] I. Saedi, S. Mhanna, and P. Mancarella, "Integrated electricity and gas system studies: Electrification of residential heating in victoria," Future Fuels CRC, Tech. Rep.

[14] AEMO, "2020 integrated system plan," www.aemo.com.au, 2020, Online, Accessed on 2023-07-07.

[15] AEMO, "2020 integrated system plan database," www.aemo.com.au, 2020, Online, Accessed on 2023-07-07.

[16] A. Xenophon and D. Hill, "Open grid model of australia's national electricity market allowing backtesting against historic data," *Sci Data*, vol. 5, 2018.

[17] NEOEN, "Victorian Big Battery," victorianbigbattery.com.au, 2023, Online, Accessed on 2023-07-07.

[18] NEOEN, "Hornsdale power reserve - south australia's big battery," www.hornsdalepowerreserve.com.au, 2023, Online, Accessed on 2023-07-07.

[19] NSW Government, "Waratah super battery," www.energyco.nsw.gov.au, 2023, Online, Accessed on 2023-07-07.

[20] AEMO, "2022 integrated system plan," www.aemo.com.au, 2022, Online, Accessed on 2023-07-07.

[21] I. Saedi, S. Mhanna, and P. Mancarella, "Integrated electricity and gas system modelling with hydrogen injections and gas composition tracking," *Applied Energy*, vol. 303, 2021.

[22] T. van Cutsem, "Artere - software for power flow computation."

[23] P. Aristidou, D. Fabozzi, and T. Van Custem, "Dynamic simulation of large-scale power systems using parallel schur-complement-based decomposition method," *IEEE Trans. on Parallel and Distributed Systems*, vol. 25, no. 10, pp. 2561–2570, 2014.

[24] G. Chaspierre, "Reduced-order modelling of active distribution networks for large-disturbance simulations," Ph.D. dissertation, Universite de Liege, Belgium, 2020.

[25] J. Vorwerk, "Integration of fast demand response into renewable power systems," Ph.D. dissertation, ETH Zürich, Switzerland, 2023.

[26] EPRI, "Specification of the Second Generation Generic Models for Wind Turbine Generators ," WECC, Tech. Rep., 2013.

[27] J. Vorwerk, U. Markovic, and G. Hug, "Fast demand response with variable speed thermal loads - towards universal modeling for stability assessment," in *2021 North American Power Symposium (NAPS)*, 2021.

[28] J. Vorwerk, U. Markovic, P. Aristidou, and G. Hug, "Quantifying the uncertainty imposed by inaccurate modeling of active distribution grids," in *2022 Power Systems Computation Conference (PSCC), Porto*, 2022.

[29] Western Electricity Coordinating Council, "WECC Battery Storage Dynamic Modeling Guideline," 2016.